Timing

Andrea Grossutti, mat. 1237344
Alessandro Lovo, mat. 1236048
Leonardo Zampieri, mat. 1237351

November 29, 2019

1 Aims

- Energy calibration of the organic scintillators and calculation of the energy resolution from the analysis of the Compton edge;
- Optimization of the external delay of the analogue CFTD to obtain the best time resolution;
- Study of the time resolution behaviour as a function of the energy;
- Comparison between the timing resolutions obtained from analogue and digital treatment of the signals;
- Measurement of the speed of light.

2 Experimental setup

The experimental setup consist of two collinear organic scintillators, mounted on a sledge, and a ^{22}Na source collimated between two lead bricks. The peaks for this source are in tab 1.

Explain better

Data are collected from the detectors through a electronic chain: a fan-in-fan-out quad module replies the signal of each detector and produces four copies of it; then, through a CFTD, a trigger signal is produced. The CFTD trigger threshold has been set so that the noise is discarded, while the interesting signals produce an output.

photopeak [keV]	Compton Edge [keV]
511.0	340.7
1274.537	1061.7

Table 1: Gamma radiation for ^{22}Na from NuDat, `https://www.nndc.bnl.gov/nudat2/decaysearchdirect.jsp?nuc=22NA&unc=nds`

3 Apparatus calibration

3.1 Calibration of DET 1 and 2

A spectra for each detector is acquired; due to the composition of the detector, the photopeaks are negligible and only the compton effect are detected. The calibration can then be done through the position of the compton edge (CE).

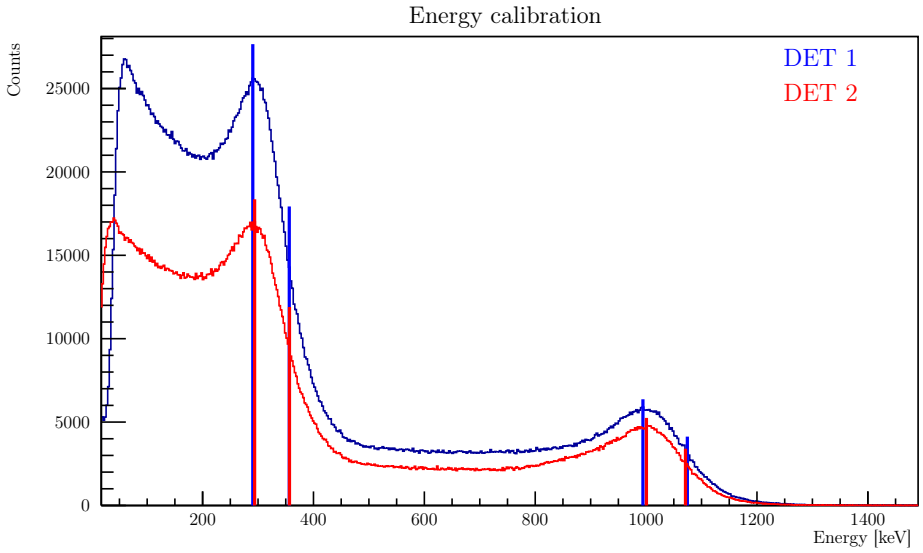

Figure 1: Position of CE's centroids and widths

The gaussian fit way was discarded, due to its strong dependence on the fit range choice. Then, after a proper spectra rebinning, for each CE the position of the maximum c_{ch} and the half width half maximum w_{ch} in channels have been found (fig 1, tab 2)*. Note that for the peak relative to the 511 keV photon the half maximum needs to be computed with respect to the baseline due to the low energy Compton events of the 1275 keV photon.
The observed CE is a convolution of a real CE with a gaussian noise whose width is proportional to the resolution of the detector σ_{res}; this convolution results in a shift of the maximum of the CE towards lower energies. By simulating† the effects on CE varying σ_{res} (fig 2) we can compute the simulated resolution $r_{sim} = \frac{w_{sim}}{c_{sim}}$ and correlate it with c_{sim}, i.e the peak position in energy (fig 3).

If we assume the calibration relation $E = a * ch + b$, then the resolution in energy is:

$$r_E = \frac{w_E}{c_E} = \frac{a w_{ch}}{a c_{ch} + b} = \frac{w_{ch}}{c_{ch} + b/a}$$

So we first assume $b/a = 0$ to compute r_E, and then by imposing $r_E = r_{sim}$ we can find the peak positions in energy $c_E = c_{sim}(r_{sim})$ allowing us to compute a and b via linear fit. We can now update the value of r_E and repeat the process. After a few iterations the process converges and gives us the results in tab 3.

*As described in Dietze, Klein: *Gamma-calibration of NE 213 scintillation counters*, Nuc. Instr. and Meth., 193 (1982), `https://doi.org/10.1016/0029-554X(82)90249-X`

†We used the formulas from N. Kudomi *Energy calibration of plastic scintillators for low energy electrons by using Compton scattering of γ rays*, Nuc. Instr. and Meth., 430 (1999), `www.elsevier.nl/locate/nima`

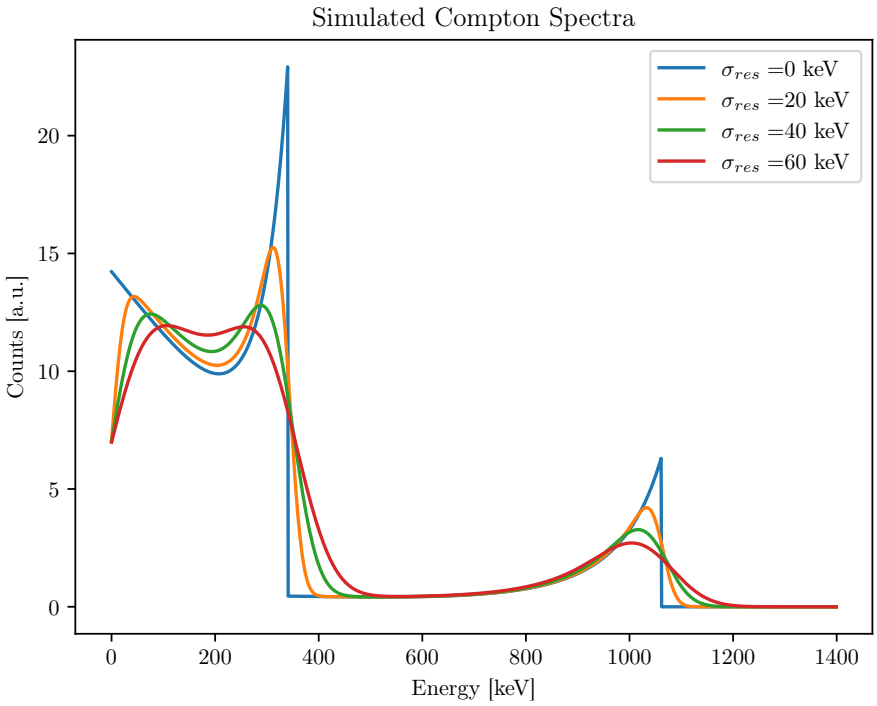

Figure 2: Simulated Compton spectra with different values of σ_{res} ($\sigma_{res} = 0$ is the real spectrum). Even if here the two peaks are represented together, they were analized independently.

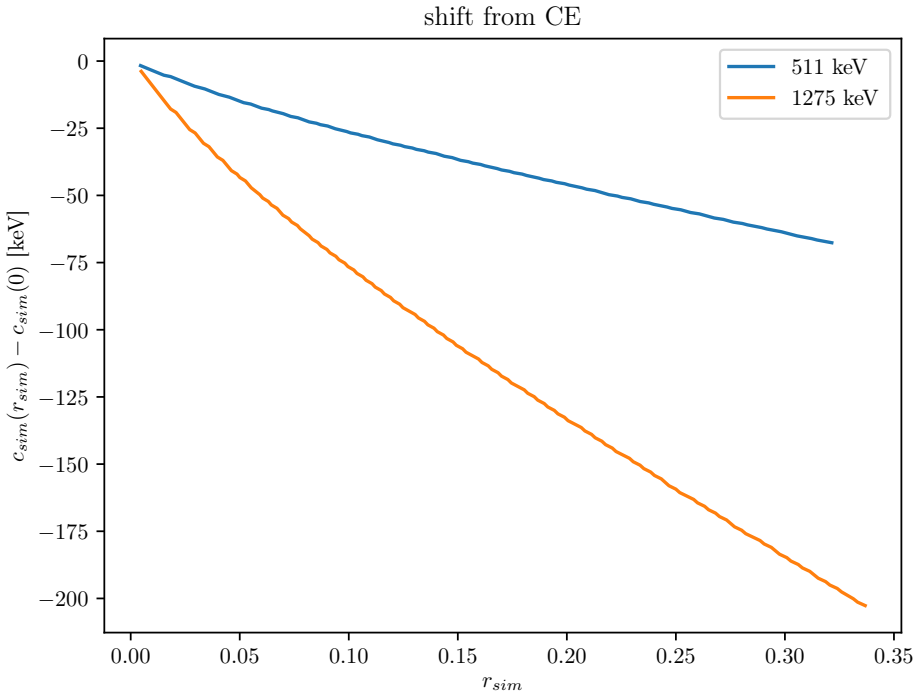

Figure 3: Relation between the resolution of the peak and the peak position

Det	p [keV]	c_{ch}	w_{ch}	c_E [keV]	w_E [keV]	r_E	σ_{res} [keV]
#1	511	3440 ± 9	736 ± 13	290.2 ± 0.7	66 ± 1	0.227 ± 0.004	38.8 ± 0.5
	1275	11312 ± 9	960 ± 13	994.1 ± 0.8	225 ± 4	0.086 ± 0.001	37.0 ± 0.5
#2	511	4400 ± 9	768 ± 13	293.8 ± 0.7	60 ± 1	0.205 ± 0.004	35.7 ± 0.6
	1275	13392 ± 9	960 ± 13	1000.5 ± 0.7	206 ± 4	0.075 ± 0.001	33.9 ± 0.5

Table 2: Centroids and widths of the CE peaks: p is the photopeak energy. The errors for the values in channels come from a uniform distribution on the bin width of the histogram. The values of c_E, w_E, r_E and σ_{res} here are the ones after the calibration process converged.

Det	a [keV]	b [keV]
#1	0.0894 ± 0.0002	-17 ± 2
#2	0.0786 ± 0.0002	-52 ± 2

Table 3: Calibrations coefficients after the calibration process converged

3.2 Calibration of the TAC

The system is set with a delay module just before the TAC's *stop*. Multiple events are acquired with different delays, and the centroid of each peak is found.

How have the centroid been found? -> A OCCHIO (mi spiace ma è la cruda realtà, non c'erano tanti altri modi visto che non erano fittabili in nessun modo (per quanto ne so io)). Anche le varianze sono a occhio ovviamente. Giuro che non mi metterò mai a costruire ponti.

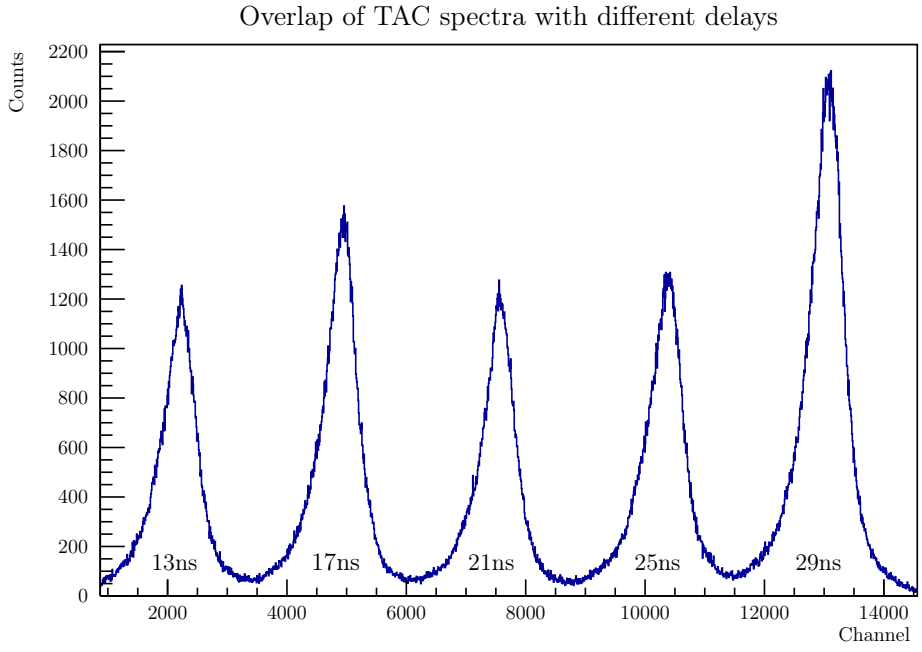

Figure 4: Different peaks with different delays.

Delay [ns]	Centroid [channel]
13	2235 ± 20
17	4950 ± 30
21	7555 ± 30
25	10390 ± 30
29	13080 ± 40

Table 4: TAC centroids. Different height of the peaks are due to different acquiring time.

The found centroid are fitted using a linear relation (the χ^2 value confirms the linear dependence):

$$t = m \cdot \text{channel} + q$$
$$m = (1.477 \pm 0.005)\text{ps}$$

where the q value isn't reported, having no meaning. In fact, delays are introduced in a more complex system, which already have an internal delay: zero external delay therefore doesn't mean zero time in TAC.

4 LEMO calibration

A set of LEMO cables is provided. Setting external delay to 13ns and inserting one by one each LEMO cable in series with the external delay module, 5-minutes datasets are acquired; computing the difference between the observed centroids and the centroid without LEMO cable previously measured, and converting it with the calibration parameter, the time-length of each LEMO cable is computed.

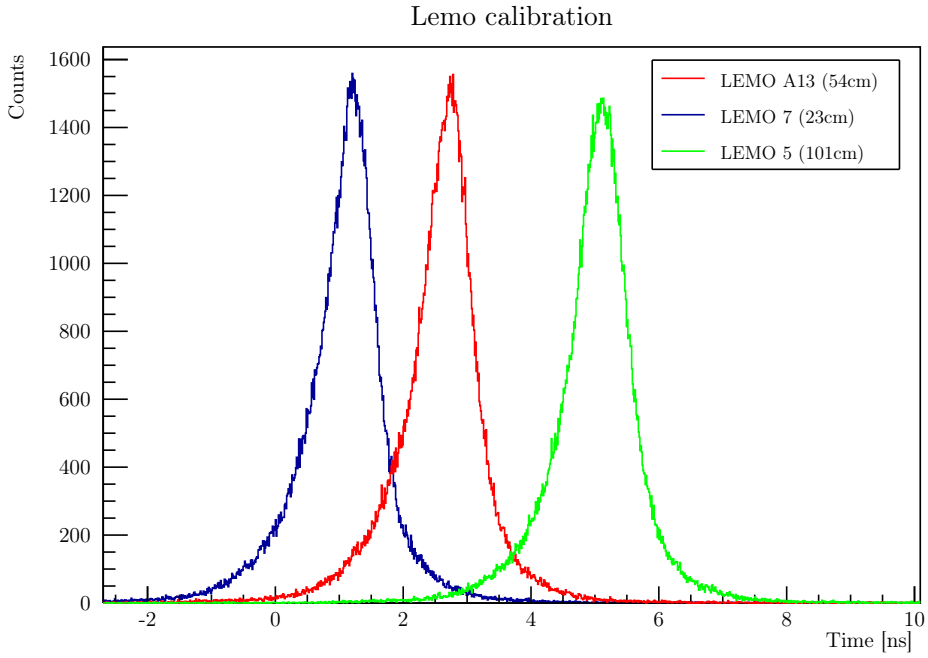

Figure 5: Some of the peaks of the LEMO cables

LEMO ID	LEMO length [cm], ±0.1	LEMO time
6	22.5	1.17 ± 0.04
7	23.0	1.15 ± 0.04
2	53.5	2.70 ± 0.03
13	53.5	2.71 ± 0.05
4	101.0	5.12 ± 0.04
5	101.0	5.08 ± 0.07

Table 5: LEMO cables

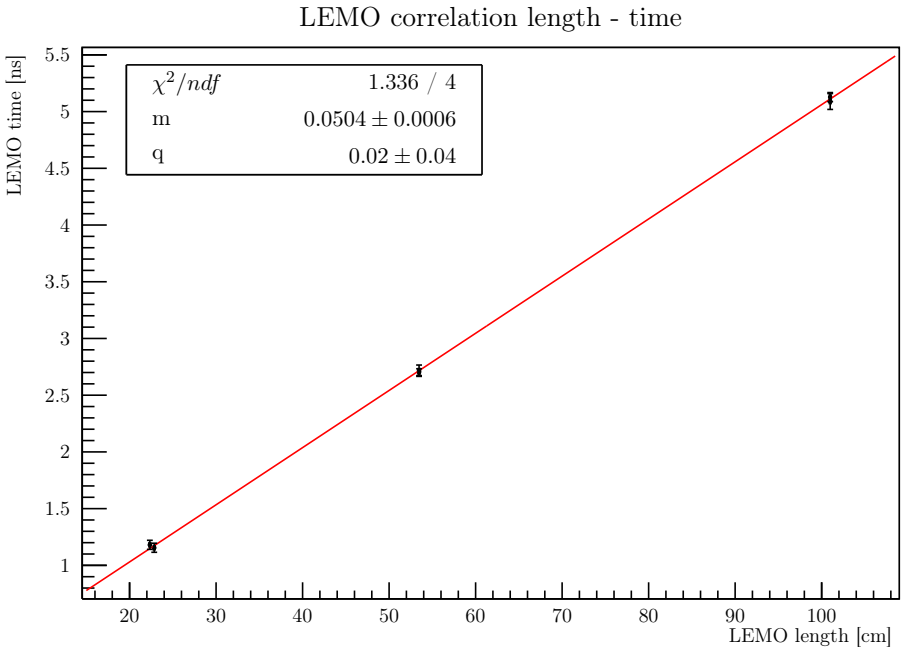

Figure 6: Relation between LEMO length and time: as expected, the dependence is confirmed.

5 CFTD delay optimization

The CFTD superimposes a delayed copy of the signal to an inverted reduced one. This delay must be properly set using LEMO cables to optimize the TAC resolution. With only the default delay, the signal detected by the TAC is large and not gaussian (see fig. 7); after some tests, a setup which lead to a better resolution and a more gaussian-like output is obtained.

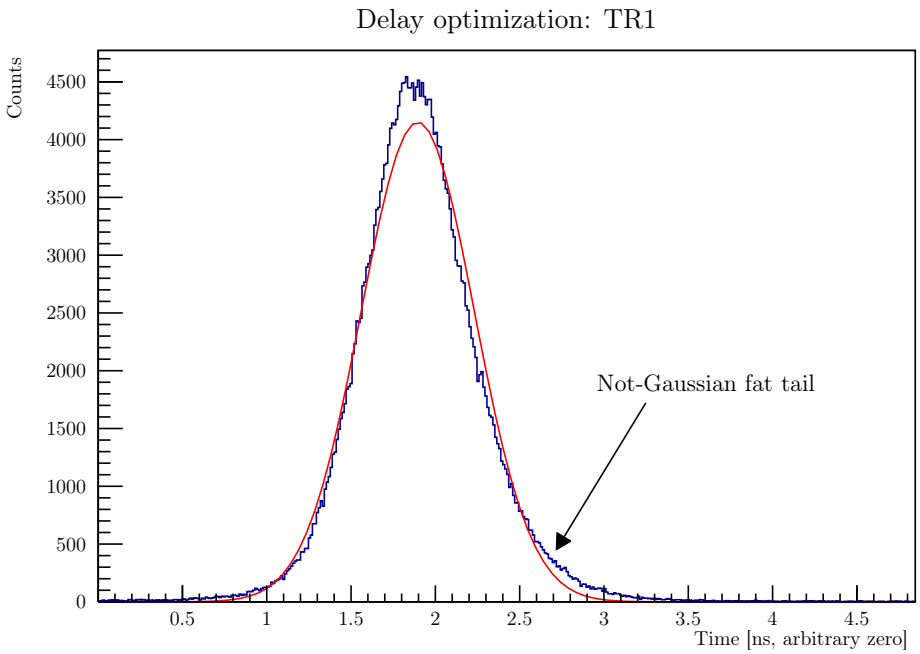

Figure 7: Initial situation: large not-guassian shape.

Different combination of LEMO cable have been inserted in series with the pre-set delay; every time the configuration changed, the WALK ADJ potentiometer has been regulated to minimize the dispersion (see fig. 8) at the zero-crossing point of the signals.

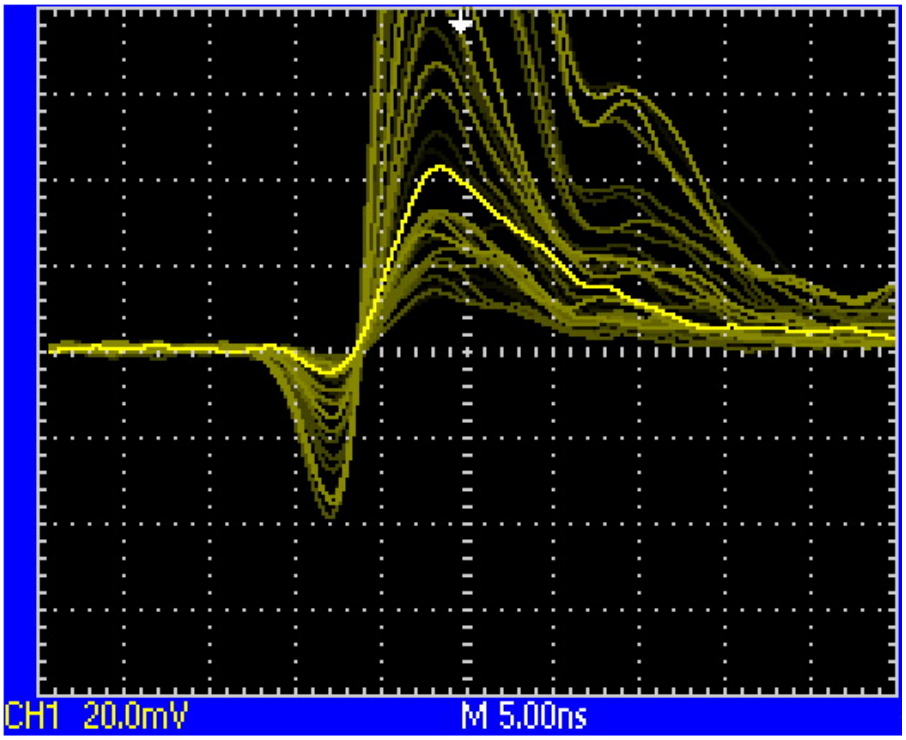

Figure 8: Monitor CFTD signal triggered on CFTD output, seen by the oscilloscope.

Fitting the obtained peaks with gaussian and relating them to the delay inserted in the CFTDs (after some tests, we noticed that the optimal setup is with the same delay in both CFTDs), the figure 9 is obtained. As can be seen from the figure, a minimum is found at about 3ns of delay (LEMO 13 and 2 for detector 1 and 2, respectively). Considering the pre-set delay (around 2ns), this lead to a optimal delay of around 5ns, that is about 80% the rise time of the detector signal ($\sim$ 6ns) as expected.

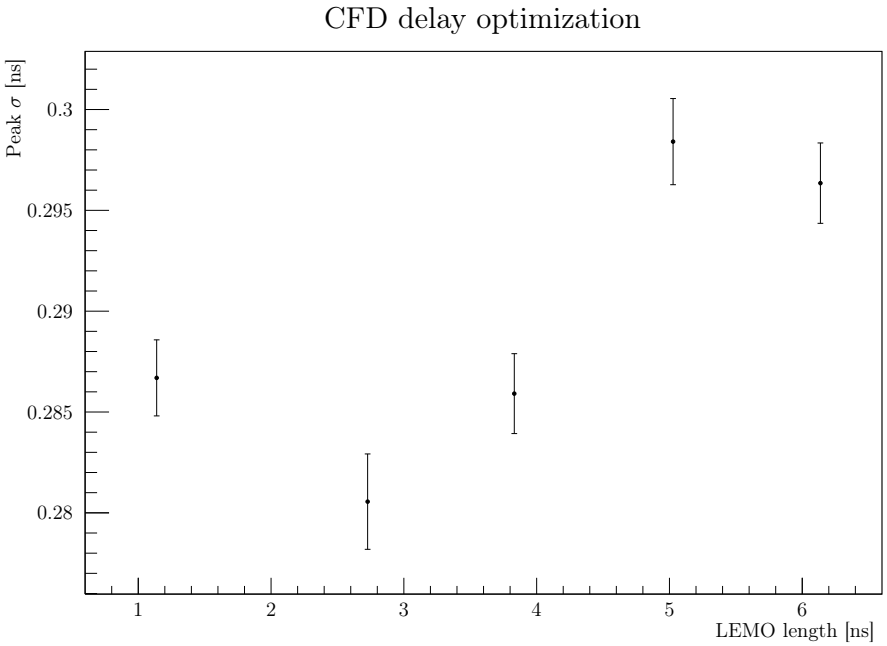

Figure 9: Optimization of the CFD delay.

The minimum configuration has been kept for all the following Measurements.

6 Time resolution in function of energy range

In order to have a wider Compton energy spectra, we acquired 20 hours of data using a ^{60}Co source. This source decays emitting two photons of energy around 1MeV: a few of them are emitted back-to-back and hence can trigger the coincidence unit (fig 10).
We can now proceed by filtering in energy the spectra and looking how the resolution of the TAC peak behaves. Since the TAC peak has a fat-tailed distribution, the gaussian fit is far from accurate, so we used the Full Width Half Maximum (FWHM) as a quantifier of the resoultion of the peaks. The filtering can be done either by setting a Lower Energy Threshold (LET) or by selecting a window in energy, i.e. keeping only the data with energy between the LET and an Upper Energy Threshold (UET). The results are shown in fig 11.

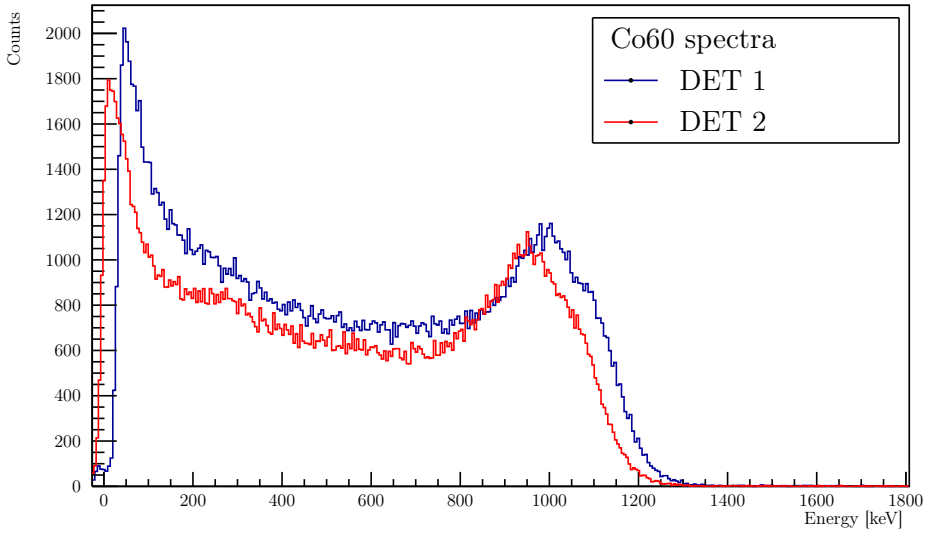

Figure 10: Energy spectra of the two detectors with ^{60}Co source.

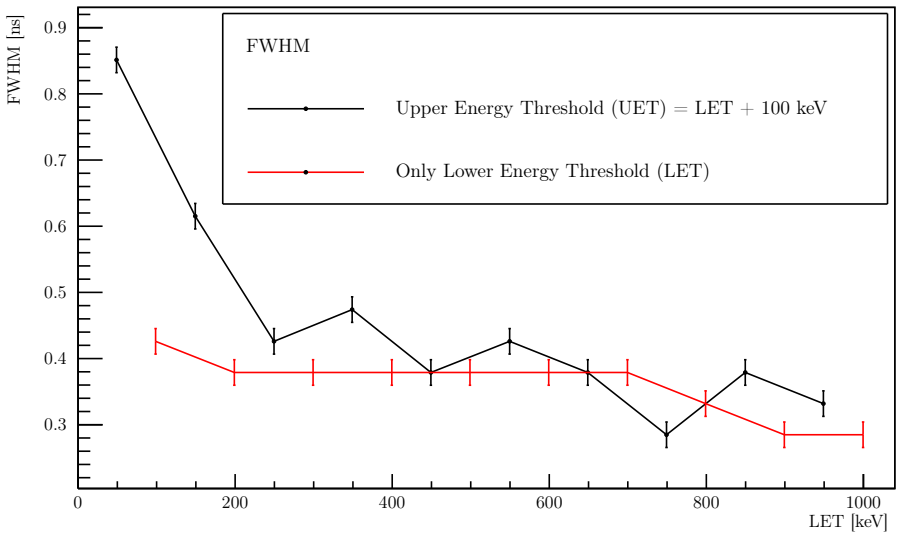

Figure 11: When computing the FWHM the peaks had been properly rebinned in order to have them sufficiently smooth. The errors on the FWHMs come from a uniform distribution on the bin width.

From fig 11 we can see that the resolution improves dramatically as we discard the events at lower energy, and then remains almost constant as the LET increases. Considering that using only a LET implies that as it increases the number of discarded data increases too, the best choice for the LET is at around 200 keV. On the other hand when using both a LET and a UET, given the shape of the ^{60}Co, moving the energy window does not drastically affect the number of discarded events. So in this case the best choice is a window near the Compton Edge.

Comment the results better

7 Speed of light

The detectors have been placed such that they're about 1.70m away. The source has been placed firstly near the detector 1 and then near the detector 2, and the TAC signal has been acquired (one hour for each configuration); therefore, the centroids μ_1 and μ_2 of the two measurements have been found through a gaussian interpolation. Measuring the distance between the two source positions d, the light speed can be computed. Observe that the two centroids have been firstly subtracted and then calibrated, to preserve the resolution.

Not clear

The errors have been propagated as statistical errors. Note the high error on the distance between the positions of the source, due to the width of the source.

$$\mu_1 = (16433 \pm 2)$$
$$\mu_2 = (8966 \pm 2)$$
$$d = (161.9 \pm 0.5)\text{cm}$$
$$c = \frac{2d}{(\mu_1 - \mu_2)m} = (2.94 \pm 0.01) \cdot 10^8 \text{m}\,\text{s}^{-1}$$

Which is the unit of μ? Channels!

8 A-Posteriori CFD

During the last day, two datasets of waveforms have been collected directly from the detectors. This allow us to simulate an a-posteriori software CFD, and compare it with the analogic one.

8.1 Waveforms

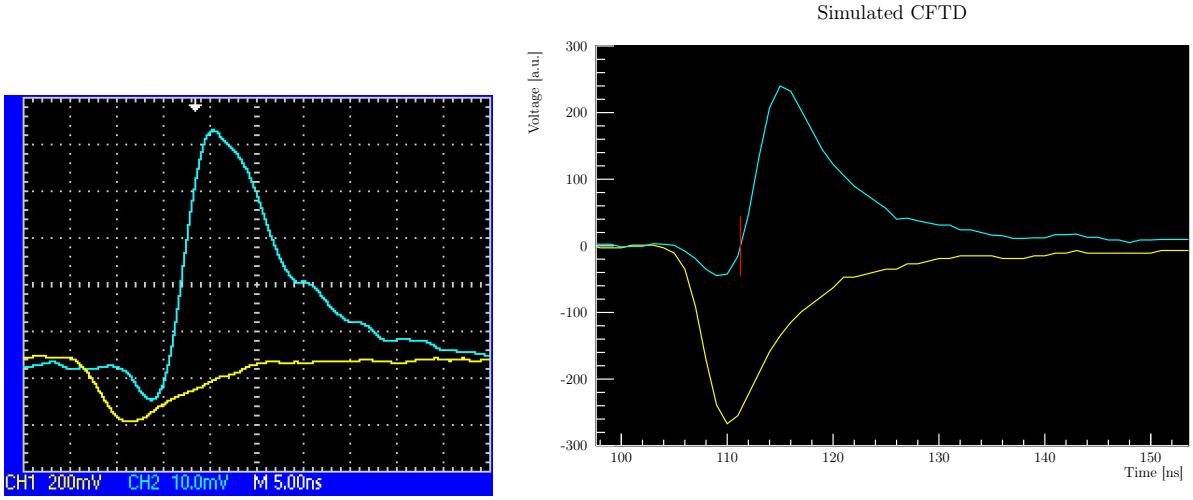

(a) Analogic CFD

(b) APosteriori CFD

Figure 12: Waveforms (yellow) and monitor signals (cyan) for analogic and software CFD, set with the same parameters (fraction = 20%, delay = $\sim$ 5ns)

As can be seen from fig. 12, the shape of waveform and signal is similar for the two system. Rise time (about 6ns) and falling time (about 20ns) are the same. The signal, however, is very short in time and the low time resolution of the digitizer (a sample each 1ns) result in a rougher waveform.

8.2 Energy spectra

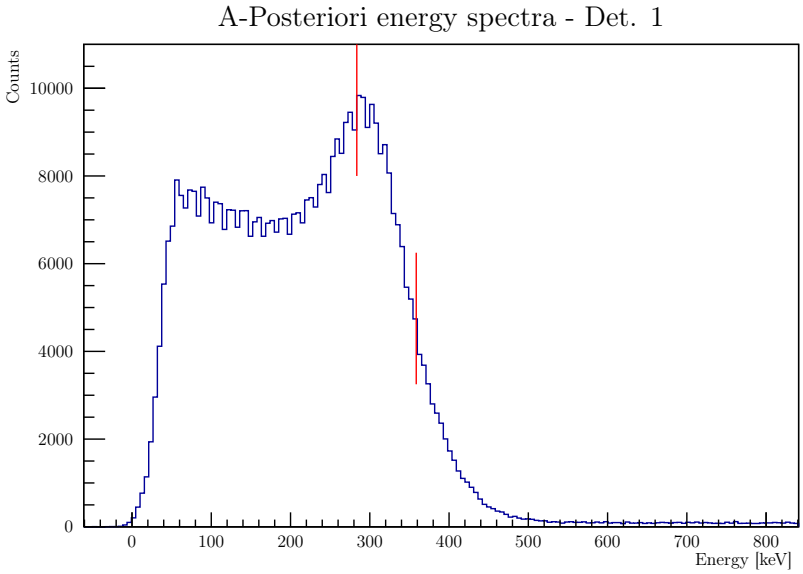

Figure 13: APosteriori energy spectra.

Integrating the waveform (substracted of the baseline) over the domain, an energy spectra can be computed. As can be seen comparing fig. 13 with fig. 1, here only the 511keV peak is visible: the

trigger set on coincidences and the low acceptance of the digitized cut away the higher peak.

Even with only one peaks, the comparison with the previous calibration permit us to make a rough calibration using position of peak and half maximum (in red in figure).

Note that in this plot there are some energy that are below zero; this is due to the combination between the low trigger threshold and the detectors resolution, the convolution of which result in a tail in negative energies.

8.3 CFD parameters

For each dataset, the following procedure is followed:

- Coincidences are searched, i.e. events that are recorded by both the detectors;
- For each event, a simulated CFD is applied to the two waveforms and zero crossing are computed;
- For each event, the time difference between the zero crossings in the two detector is computed;
- The distribution of the time difference is builded: mean, full with at half maximum (FWHM) and kurtosis (a measure of the *gaussianity* of the distribution, equals 0 for a perfect gaussian) are computed;

This procedure is repeated for different combination of CFD delay (from 1 to 10ns, with 0.25ns step) and attenuation fraction (from 0.1 to 0.9, with 0.1 step) and the plots of FWHM and kurtosis are builded.

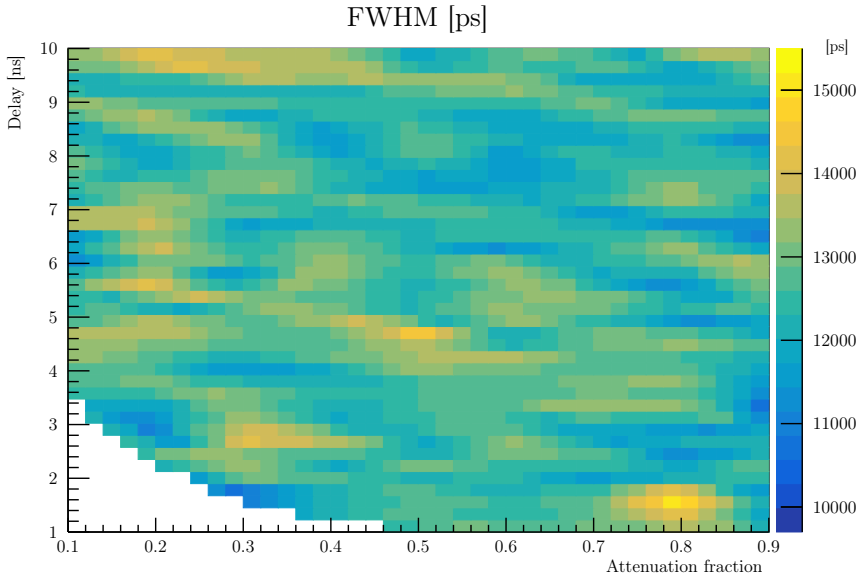

Figure 14: FWHM of the time differences distribution as function of CFD parameters.

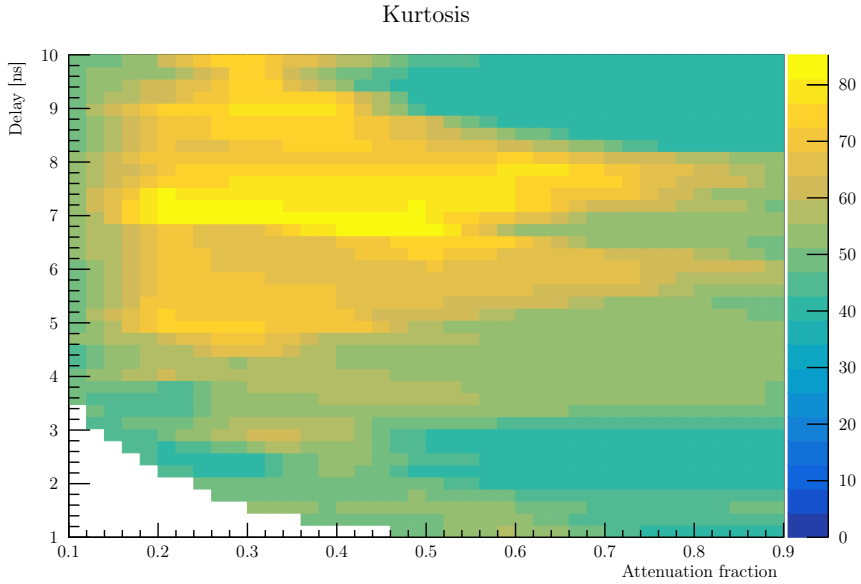

Figure 15: Kurtosis of the time differences distribution as function of CFD parameters.

Note that the low-delay low-fraction corner points has been discarded: their means result incompatible with the others and their FWHM extremely high, reflecting errors (probably due to low digitizer time resolution) in zero-crossings finding.

The kurtosis values are very high: plotting one of the distribution, it's clear they aren't gaussian-like, but triangular-like, again because of digitizer resolution. It records only 5-6 points in the rising time, digitally sampled; the zero crossing is therefore individuated by interpolating two (or in very good conditions four) points: a very rough interpolation! Assuming the uniform probability density function (PdF) typical of digital instruments and convolving the start and stop PdF, they result in a triangular-like PdF as experimental results show.

8.4 Time resolution and energy threshold